Research Article | Vol. 34, No. 23 / 16 Nov 2026 / Optics Express 43532
Optics EXPRESS

Single-mode, distributed feedback interband cascade lasers grown on GaSb and GaAs substrates, emitting at 4.6 µm

LYDIA KACEL,[1,2,3] ZEINEB LOGHMARI,[2] DANIEL ANDRES DIAZ-THOMAS,[1] MAËVA FAGOT,[1] JULIE GOUTORBE,[1] ALEXEI BARANOV,[1,2] ROLAND TEISSIER,[2] AND LAURENT CERUTTI[1,*]

[1]*IES, Univ. Montpellier, CNRS, 34000 Montpellier, France*
[2]*MirSense, Orsay, France*
[3]*Lydia.Kacel@mirsense.com*
[*]*laurent.cerutti@umontpellier.fr*

Abstract: In this work, single-mode, interband cascade lasers (ICLs) incorporating a metal top-surface distributed feedback (DFB) grating are successfully demonstrated on both native GaSb and lattice-mismatched GaAs substrates. To the best of our knowledge, this work represents the first demonstration of single-mode DFB operation near 4.6 µm from an ICL grown on a lattice-mismatched GaAs substrate. First-order gratings etched into the upper InAs/AlSb cladding are integrated with 6-µm-wide and 2-mm-long ridge waveguides. ICLs are studied under pulsed operation up to 60°C. Comparable performance is achieved for both substrate platforms, with threshold current densities of 500 A/cm^2 at 20 °C. Single mode operation with side mode suppression ratio (SMSR) exceeding 20 dB is obtained for temperatures above 30°C. The devices emit at 4.6 µm, a wavelength relevant for carbon monoxide (CO) spectroscopy.

Published by Optica Publishing Group under the terms of the Creative Commons Attribution 4.0 License. Further distribution of this work must maintain attribution to the author(s) and the published article's title, journal citation, and DOI.

1. Introduction

The mid-infrared (MIR) spectral region, spanning 2 - 20 µm [1] is characterized by strong molecular absorption features and atmospheric transparency windows [2] making it attractive for such applications as environmental monitoring, spectroscopy [3,4], medical diagnostics [5], free space communications [6], security and defense [7,8]. To meet these application requirements, different MIR light sources have been developed [1]. Sb-based type-I quantum well diode lasers [9] are efficient for wavelength below 3 µm, whereas quantum cascade lasers (QCL) [10,11] provide superior performance beyond 5 µm. In the intermediate range of 3 - 6 µm, interband cascade lasers (ICLs) have demonstrated excellent performance [12,13]. Owing to their hybrid design combining interband transitions with a cascade architecture, ICLs exhibit low threshold current densities, low power consumption, high quantum efficiency and a wide spectral tunability [14–16]. These properties make ICLs well suited for compact and energy-efficient MIR light sources.

However, the use of ICLs in commercial applications, such as trace gas detection and industrial process monitoring, is limited by the small diameter and costly GaSb or InAs substrates. A promising strategy is to grow ICLs on technological substrates such as GaAs or Si. These substrates offer advantages in terms of wafer size, scalability, compatibility with established semiconductor manufacturing technologies, which could reduce fabrications cost. Nevertheless, the epitaxial growth of III-Sb materials on GaAs is challenging due to the large lattice mismatch of approximately 8%. This mismatch results in a high density of threading dislocations propagating

#614197 https://doi.org/10.1364/OE.614197
Journal © 2026 Received 12 Aug 2026; revised 7 Oct 2026; accepted 12 Oct 2026; published 3 Nov 2026

Optics EXPRESS

throughout the epitaxial structure. These crystalline defects act as non-radiative recombination centers, leading to reduced efficiency and degraded device reliability [17,18].

Consequently, the design of an active region tolerant to dislocations is critical. Type-II Sb-based ICLs exhibit a band structure that suppresses non-radiative recombination associated with dislocations and therefore show strong potential to address this challenge [19]. Recent studies comparing ICLs grown on GaSb, GaAs, and Si [20,21] have demonstrated that high device performance can be preserved despite significant lattice mismatch and high dislocation densities. The defect tolerance highlights the structural robustness of ICLs and supports their suitability for integration on cost-effective technological substrates.

In addition, many MIR applications, particularly gas sensing, require stable single-mode operation to ensure high wavelength selectivity and accurate detection. One approach relies on distributed feedback (DFB) lateral gratings, in which metallic periodic structures are implemented on both sides of the laser ridge, typically at the level of the GaSb separate confinement layer (SCL) [22,23]. This configuration has demonstrated a single-mode emission up to 5 µm with SMSR exceeding 30 dB. An alternative design consists of corrugated-sidewall gratings, where periodic modulation of the ridge sidewalls provides both lateral mode suppression and longitudinal mode selection. Using this approach, stable single-mode operation around 3.6 µm was achieved up to 30 °C [24]. A third configuration is based on top-surface DFB gratings, typically realized by depositing a high-refractive-index germanium (Ge) layer on top of the laser ridge, and subsequently patterning it to define the grating [25–27]. This design has enabled continuous-wave (CW) single-mode emission around 3.7 µm, with an SMSR of up to 30 dB and thermal stability up to 80 °C.

In this work, an alternative top surface configuration based on a metal grating was investigated. This architecture was selected because it relies on a mature and well controlled fabrication process previously developed for InAs/AlSb QCLs [28,29]. However, using this approach, to the best of our knowledge, single-mode DFB operation near 4.6 µm has not previously been reported for ICLs grown on lattice-mismatched GaAs substrates. In this study, we report the design, fabrication and characterization of single-mode ICLs emitting at 4.6 µm, for carbon monoxide (CO) detection, grown on both GaSb and GaAs substrates. GaAs substrates provide a cost-effective alternative to GaSb, with the additional advantage of larger wafer diameters. Both devices incorporate a top-surface metallic DFB grating etched in the InAs/AlSb cladding layer. The resulting DFB ICLs exhibit single-mode operation up to 60°C in pulsed operation. Pulsed operation was used to limit the average electrical power dissipated in the device and minimize heating during the operation. These results demonstrate the potential for compact, energy-efficient, high-performance gas sensing system based on ICLs grown on mismatched substrates.

2. ICL structure

The ICL structures were grown by solid-source molecular beam epitaxy (MBE) simultaneously on GaSb substrate and on a GaSb-on-GaAs template. The wafers used in the present study are the same as those reported in Ref. [21] .The structure consists of seven active stages designed to emit at 4.6 µm, enclosed between two 500 nm-thick Te-doped GaSb SCLs. The top and bottom n-type claddings consist on InAs/AlSb superlattices with thicknesses of 1.9 and 3.1 µm, respectively.

3. DFB design

To achieve single-mode emission in both transverse and longitudinal directions, two modeling steps were performed using COMSOL Multiphysics [30]. The first step of the study focused on the transverse optical confinement required to suppress higher-order lateral modes (TE_{01}). The modeling structure, illustrated in Fig. 1.a, includes the laser active region, the optical confinement layers, the top metal contact, and the lateral insulation regions. The optical properties of

Optics EXPRESS

the different materials, including the refractive index n and the extinction coefficient k, were experimentally determined by ellipsometry measurements. For Ti and Au, the corresponding values of n and k at 4.6 µm were taken from Refs. [31,32]. All the optical parameters used in the simulations are summarized in Table 1.

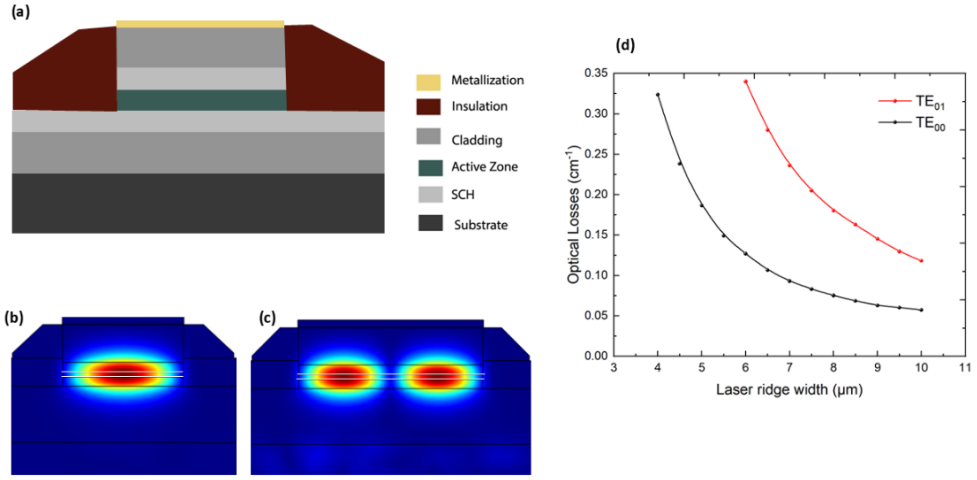


Fig. 1. (a) Simulated waveguide structure used for optical modeling. (b) Optical field distribution of the fundamental TE_{00} mode in a 5 µm-wide ridge waveguide. (c) Optical field distribution in a wider ridge (8 µm) waveguide showing the simultaneous excitation of multiple transverse modes. (d) Calculated optical losses as a function of laser cavity width for the two TE modes: fundamental TE_{00} (in black) and higher order TE_{01} (in red).

Table 1. Optical properties of the different materials

Materials	n	k
Au	2.95	33.31
Ti	2.69	8.03
Cladding	3.36	0
SCH	3.77	0
Active zone	3.55	0

A parametric study of the ridge width (w) was carried out to evaluate the optical losses for the fundamental (TE_{00}) and first-order (TE_{01}) transverse modes. The simulated optical field distributions of the TE_{00} for a 5 µm ridge width and TE_{01} modes of 8 µm are presented in Figs. 1.b and 1.c, respectively. The evolution of the optical losses for the two modes, TE_{00} (black) and TE_{01} (red), shown in Fig. 1.d, indicates that a ridge width of 6 µm provides a good compromise. At this width, the optical losses of the fundamental TE_{00} mode remain low, while those of the higher-order TE_{01} mode increase significantly, thereby promoting stable single-transverse-mode operation.

Based on these results, a ridge width of 6 µm was selected to ensure robust single-mode guiding in the transverse direction.

For longitudinal single-mode emission, a second modeling stage was carried out. A metallized DFB grating was implemented on the top surface of the laser ridge. The Bragg grating introduces a periodic modulation of the refractive index [29,30,33] inducing selective reflection at wavelength

Optics EXPRESS

defined by Bragg's condition:

$$\lambda_B = \frac{2\Lambda}{m} n_{\text{eff}} \tag{1}$$

Where λ_B is the Bragg wavelength, m *is* the diffraction order, n_{eff} is the effective refractive index and Λ *is* the grating period. A first-order Bragg grating (m = 1) was chosen for its stronger coupling efficiency compared to higher-order gratings [34]. For an effective refractive index of 3.56 estimated from prior experiments, the required grating period was calculated to be 649 nm grating to achieve single-mode emission at 4.6 µm. The simulated structure is shown in Fig. 2.a. The grating consists of a regular modulation of the effective refractive index along the laser cavity. The simulation parameters include the thickness of the top cladding layer, the etching depth of the grating, and the actual geometric profile obtained by the process. Due to the specific etching conditions of the InAs/AlSb superlattice, the etched patterns exhibit a trapezoidal geometry with an angle of approximately 120°. The trapezoidal etch profile was included in the grating design, with the target duty cycle of 60% defined at half the grating depth. The analysis of the optical field distribution showed two distinct modal configurations. The semiconductor mode is mainly confined below the top cladding layer, which limits its interaction with the metallic contact and therefore reduces absorption losses. In contrast, the metal mode exhibits greater penetration of the electromagnetic field toward the top metal contact. This increased overlap with the metal layer results in higher optical absorption losses. The simulation results further show that these losses increase monotonically with the etching depth of the grating, as illustrated in Fig. 2.b. To maintain a low threshold current density, the optical losses of both modes must remain low. However, a sufficient loss difference between the semiconductor mode and the metallic mode is required to ensure effective mode discrimination.

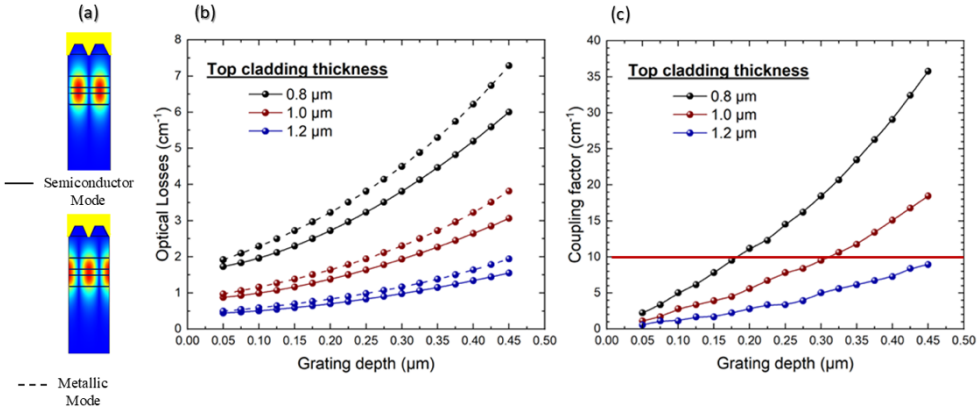


Fig. 2. (a) Cross-sections showing the semiconductor mode and metallic mode. (b) Variation of the optical losses with grating etch depth. (c) Evolution of the coupling coefficient with grating etching depth for various top cladding thicknesses ranging from 0.8 to 1.2 µm.

The coupling factor between the DFB grating and the optical mode in the active zone is described by the complex coupling factor κ:

$$\kappa = \frac{\Delta\omega}{2c} n_{eff} + i\frac{\Delta\alpha}{2} \tag{2}$$

where Δω is the frequency difference, Δα the loss difference between the semiconductor and metallic modes, and c is the speed of light in the vacuum. Since the imaginary component accounts for less than 0.2% of the calculated coupling coefficient only the real part of the coupling factor is considered hereafter [35]. Figure 2.c illustrates the evolution of the coupling coefficient

Optics EXPRESS

κ with the gratings etching depths, for different top cladding thicknesses ranging from 0.8 to 1.2 µm.

The coupling factor κ increases with grating etch depth and decreases with increasing top cladding thickness. Previous studies [23,24] suggest that the product κL close to 2 provides a suitable initial compromise for single-mode operation, where L is the DFB grating length. In the present devices, the grating extends over the entire laser cavity, such as L = 2 mm. Therefore, a coupling coefficient of approximately 10 cm^{-1} was selected as a design target, as indicated by the red line in Fig. 2.c.

Based on the simulation of the modal losses and the grating coupling factor presented in Figs. 2.b and 2.c a top cladding thickness of 1 µm was selected as a compromise between low modal losses and adequate confinement of the optical mode. The grating etch depth was set to 350 nm, yielding to a grating coupling coefficient of 10 cm^{-1} and an etch depth compatible with the fabrication process with a ridge width of 6 µm. Together, these design parameters enable stable single-mode emission at 4.6 µm.

4. DFB ICL fabrication

Two identical fabrication processes were implemented on ICL structures grown on native GaSb and lattice mismatched GaAs substrates. Both devices were processed using the same fabrication steps to ensure comparable geometry and optical design. First, the initial 1.9 µm-thick upper cladding was thinned to 1 µm using inductively coupled plasma reactive ion etching (ICP-RIE) with a Cl_2/Ar gas mixture. This step was monitored on a simultaneously processed reference sample by profilometry, with an estimated accuracy of ±40 nm. The DFB grating had a period of 649 nm and an etched-trench width of approximately 260 nm. The grating was then defined by electron-beam lithography (E-beam) and subsequently transferred into the InAs/AlSb top cladding using the same etching process as for the upper-cladding thinning step.

The laser ridge, with a width of 6 µm, was defined by optical photolithography followed by dry etching. Electrical isolation was achieved using a baked positive resist (AZ1518), and Ti/Au was deposited to form the top electrical contact. The substrates were then mechanically thinned to 200 µm and metallized with a Pd/AuGeNi stack to form the bottom contact. Finally, the wafers were cleaved into individual laser and soldered epitaxial side-down onto Au coated AlN submounts using In. The laser facets were left uncoated. Figure 3 shows a scanning electron microscope (SEM) image of a DFB ICL fabricated on GaAs substrate at the end of the process.

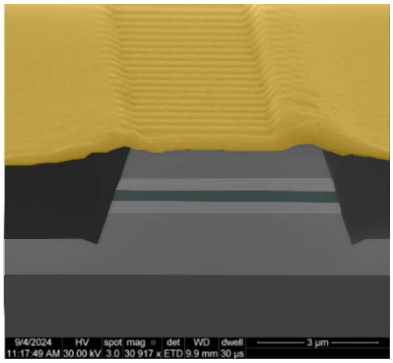


Fig. 3. SEM image of DFB-ICL grown onto GaAs substrate.

Optics EXPRESS

5. ICL performance analysis

Figures 4.a and 4.b show the light-current-voltage (L–I–V) characteristics measured at different temperatures for DFB ICLs grown on GaSb and GaAs substrates, respectively. Measurements were carried out under pulsed operation using 310 ns current pulses at a repetition rate of 12 kHz, corresponding to a duty cycle of 0.37%. The pulse duration was selected to limit device self-heating during the measurement, especially for the GaAs-base device, which exhibits a higher operating voltage and series resistance. The lasers were characterized up to 60°C, which corresponds to the maximum temperature accessible with the present experimental set-up.

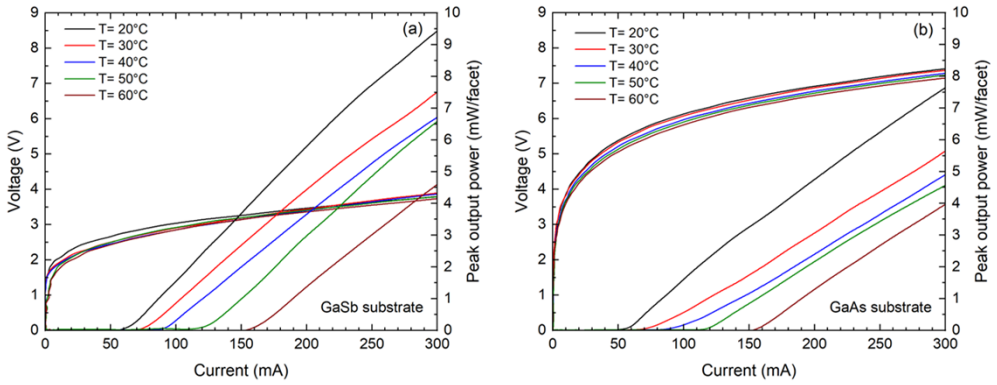


Fig. 4. L-I-V characteristics at different temperatures (20°C to 60°C) grown on GaSb (a), and GaAs (b) substrates.

Despite the different substrates, DFB ICLs grown on GaSb and GaAs exhibit similar performance. The threshold currents are comparable, around 60 mA at 20°C. The DFB ICLs exhibit a characteristic temperature T_0 of 42 K and 41 K on GaSb and GaAs, respectively, compared with 41 K for the corresponding Fabry-Pérot ICLs on both substrates [21]. These similar values indicate that the DFB technology does not affect the thermal performance of the devices. The single-facet slope efficiency is approximatively 0.05 W/A and 0.04 W/A for the ICLs on GaSb and GaAs, respectively. This difference may result from a combination of device-to-device variations in the reflectivity of the uncoated cleaved facets, the higher series resistance of the ICLs grown on GaAs.

The external differential quantum efficiency, defined as:

$$\eta_d = \frac{q}{h\,\nu}\frac{\Delta P}{\Delta I} \tag{3}$$

where q is the elementary charge, h is Planck's constant, and $\nu = c/\lambda$ is the optical frequency. The two facet-external differential quantum efficiencies of 37% and 28% for the ICLs grown on GaSb and GaAs, respectively. The corresponding wall-plug efficiencies at 300 mA and RT are 1.66% and 0.74%, respectively. The lower differential efficiency of the GaAs-based device may result from a combination of several effects, including defect-related nonradiative recombination associated with the dislocations present in the GaAs-based epitaxial structure, higher internal optical losses, and enhanced self-heating due to its higher series resistance. These effects can reduce the carrier-to-photon conversion efficiency and, consequently, the external differential quantum efficiency. Furthermore, these values remain lower than the 82% reported for Fabry–Perot ICLs fabricated from the same heterostructure [21]. The reduction is attributed to the relatively strong coupling ($\kappa \cdot L \sim 2$) and the detuning between the Bragg mode and the gain peak at 4.7 µm, both of which limit the extracted output power and overall efficiency.

Optics EXPRESS

The I-V characteristics differ between the two devices. At an injection current of 200 mA, the DFB ICL on GaSb exhibits a bias voltage of 3.5 V, whereas the ICL grown on GaAs reaches 6.5 V. The higher operating voltage of the ICL on GaAs is attributed to the regions below the lower cladding, including possible contributions from the GaAs/GaSb interface and the bottom electrical contact. Indeed, the contact configuration differs from the top-to-top geometry employed in previous studies [19–21] in which the lower contact was formed in the InAs/AlSb lower cladding using Ti/Au metallization. In the present configuration top-to-bottom configuration, the bottom contact was deposited on the backside of both the GaSb and GaAs susbtrates using Pd/AuGeNi stack. Achieving low resistance ohmic contacts with this metallization requires thermal annealing to facilitate Au diffusion. On GaSb, effective diffusion occurs at ~ 200°C [36], while on GaAs higher temperatures (> 450°C) are needed [37]. Such high temperature treatment can degrade the laser structure, limiting the annealing temperature and preventing formation of a low-resistance contact on GaAs. Consequently, contact resistance is higher, resulting in increased operating voltage.

Figures 5.a and 5.b show the emission spectra of DFB ICL lasers grown on GaSb and GaAs substrates, respectively, measured at 200 mA for temperatures ranging from 20 °C to 60 °C.

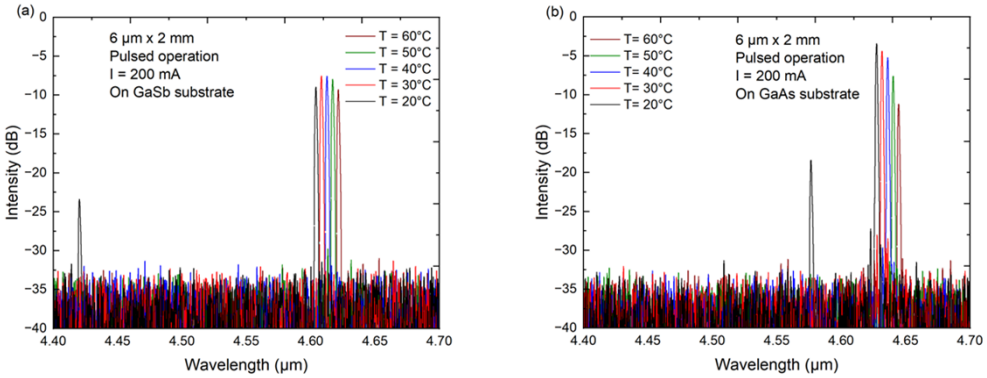


Fig. 5. Emission spectra of DFB ICL grown on GaSb and GaAs substrates at 200 mA for heat-sink temperature from 20 to 60°C.

In both cases, single-mode operation with a SMSR above 20 dB was observed at temperature above 30°C, giving a temperature tuning coefficient of 0.55 nm/°C. At temperature of 20°C, an SMSR of approximately 16 dB was obtained. The measured SMSR values demonstrate the suitability of the DFB ICLs for spectroscopic applications.

Figure 6 shows the emission wavelength as a function of injection current for temperatures between 20°C and 60°C, for both substrates: GaSb (solid lines) and GaAs (dashed lines).

The emission wavelength increases with injection current under pulsed operation. An average current-tuning coefficient of 0.005 nm/mA was obtained from a linear fit to the measured wavelength-versus-current data. For the GaSb-based devices, the emission wavelength ranges from approximately 4.599 µm at 20 °C to 4.617 µm at 60 °C, corresponding to a temperature tunability of approximately 8 cm^{-1}. A similar tuning range is observed for GaAs-based devices, with the wavelength shifting from approximately 4.627 µm to 4.645 µm.

Optics EXPRESS

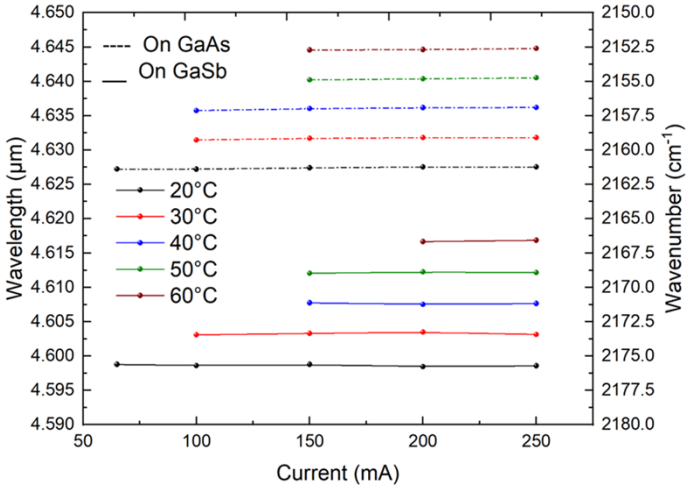


Fig. 6. Emission wavelength as a function of injection current at different heat-sink temperatures for the DFB ICLs grown on GaSb (solid lines) and GaAs (dashed lines).

6. Conclusion

Single-mode DFB ICLs emitting near 4.6 µm were designed, fabricated, and characterized on both native GaSb and lattice-mismatched GaAs substrates. The devices incorporated first-order top-surface metal gratings etched directly into the upper InAs/AlSb cladding and exhibited stable single-mode operation up to the maximum investigated heat-sink temperature of 60 °C under pulsed excitation. Despite its higher series resistance, the GaAs-based device showed threshold and spectral characteristics comparable to those of the reference device grown on GaSb. A side-mode suppression ratio of at least 20 dB was maintained over the investigated operating range, and wavelength tuning from 4.601 to 4.618 µm was achieved without mode hopping. The demonstration of single-mode DFB operation on lattice-mismatched GaAs at this wavelength represents an important step toward lower-cost mid-infrared laser sources for CO spectroscopy.

Funding. Agence Nationale de la Recherche (ANR-11-EQPX-0016, ANR-21-ESRE-0026, ANR-25-LCV2-0018); European Commission (101135764 - EVOQUE).

Acknowledgment. This work was partially supported by the French National Research Agency (ANR) through project the LabCom ANR CASIMIR (ANR-25-LCV2-0018) the France 2030 program, managed by the National Research Agency under the Equipex EXTRA and HYBAT (ANR-11-EQPX-0016 and ANR-21-ESRE-0026) and the European Union's Horizon Europe research and innovation program (101135764 - EVOQUE). This work was done within the Centrale de Technologie en Micro et Nanoélectronique de Montpellier and partly supported by the RENATECH(+) network

Disclosures. The authors declare no conflicts of interest.

Data availability. Data underlying the results presented in this paper are not publicly available at this time but may be obtained from the authors upon reasonable request.

References

1. S. J. Sweeney, T. D. Eales, and I. P. Marko, "The physics of mid-infrared semiconductor materials and heterostructures," *Mid-infrared Optoelectronics*, Elsevier, pp. 3–56 (2020).
2. Z. Zhao, B. Wu, X. Wang, *et al.*, "Mid-infrared supercontinuum covering 2.0–16 µm in a low-loss telluride single-mode fiber," Laser & Photonics Reviews **11**(2), 1700005 (2017).
3. C. Bauer, U. Willer, R. Lewicki, *et al.*, "A Mid-infrared QEPAS sensor device for TATP detection," J. Phys.: Conf. Ser. **157**, 012002 (2009).
4. E. Tütüncü, M. Nägele, P. Fuchs, *et al.*, "iHWG-ICL: Methane Sensing with Substrate-Integrated Hollow Waveguides Directly Coupled to Interband Cascade Lasers," ACS Sens. **1**(7), 847–851 (2016).

Optics EXPRESS

5. Á. I. López-Lorente and B. Mizaikoff, "Mid-infrared spectroscopy for protein analysis: potential and challenges," Anal. Bioanal. Chem. **408**(11), 2875–2889 (2016).
6. P. Didier, H. Knötig, O. Spitz, *et al.*, "Interband cascade technology for energy-efficient mid-infrared free-space communication," Photonics Res. **11**(4), 582 (2023).
7. M. B. Pushkarsky, I. G. Dunayevskiy, M. Prasanna, *et al.*, "High-sensitivity detection of TNT," Proc. Natl. Acad. Sci. U. S. A. **103**(52), 19630–19634 (2006).
8. N. S. Prasad, "Optical Communications in the mid-wave IR spectral band," *Free-Space Laser Communications*, Springer New York, pp. 347–391 (2005).
9. L. A. Coldren, S. W. Corzine, and M. L. Mašanović, *Diode Lasers and Photonic Integrated Circuits*, 1 ed., Wiley (2012).
10. J. Faist, F. Capasso, D. L. Sivco, *et al.*, "Quantum Cascade Laser," Science **264**(5158), 553–556 (1994).
11. E. Tournié and A. N. Baranov, "Mid-Infrared Semiconductor Lasers," *Semiconductors and Semimetals*, Elsevier, pp. 183–226 (2012).
12. R. Q. Yang, "Infrared laser based on intersubband transitions in quantum wells," Superlattices Microstruct. **17**(1), 77–83 (1995).
13. J. Meyer, W. Bewley, C. Canedy, *et al.*, "The Interband Cascade Laser," Photonics **7**(3), 75 (2020).
14. I. Vurgaftman, R. Weih, M. Kamp, *et al.*, "Interband cascade lasers," J. Phys. D: Appl. Phys. **48**(12), 123001 (2015).
15. I. Vurgaftman, W. W. Bewley, C. L. Canedy, *et al.*, "Interband Cascade Lasers With Low Threshold Powers and High Output Powers," IEEE J. Select. Topics Quantum Electron. **19**(4), 1200210 (2013).
16. O. Graydon, "Interband cascade laser," Nature Photon **12**(10), 568 (2018).
17. W. Qian, M. Skowronski, R. Kaspi, *et al.*, "Nucleation of misfit and threading dislocations during epitaxial growth of GaSb on GaAs (001) substrates," J. Appl. Phys. **81**(11), 7268–7272 (1997).
18. J. Jiménez, "Laser diode reliability: crystal defects and degradation modes," Comptes Rendus. Physique **4**(6), 663–673 (2003).
19. L. Cerutti, D. A. Díaz Thomas, J.-B. Rodriguez, *et al.*, "Quantum well interband semiconductor lasers highly tolerant to dislocations," Optica **8**(11), 1397 (2021).
20. M. Fagot, D. A. Díaz-Thomas, A. Gilbert, *et al.*, "Interband cascade lasers grown simultaneously on GaSb, GaAs and Si substrates," Opt. Express **32**(7), 11057 (2024).
21. M. Fagot, D. A. Díaz-Thomas, A. Gilbert, *et al.*, "High-performance GaSb-based interband cascade lasers emitting at 4.7 µm grown on GaAs and Si substrates," Opt. Mater. Express **15**(11), 2654 (2025).
22. R. Weih, L. Nähle, S. Höfling, *et al.*, "Single mode interband cascade lasers based on lateral metal gratings," Appl. Phys. Lett. **105**(7), 071111 (2014).
23. M. Von Edlinger, J. Scheuermann, R. Weih, *et al.*, "Monomode Interband Cascade Lasers at 5.2 µm for Nitric Oxide Sensing," IEEE Photonics Technol. Lett. **26**(5), 480–482 (2014).
24. C. S. Kim, M. Kim, W. W. Bewley, *et al.*, "Corrugated-sidewall interband cascade lasers with single-mode midwave-infrared emission at room temperature," Appl. Phys. Lett. **95**(23), 231103 (2009).
25. C. S. Kim, M. Kim, W. W. Bewley, *et al.*, "Single-mode distributed-feedback interband cascade laser for the midwave infrared," Appl. Phys. Lett. **88**(19), 191103 (2006).
26. C. S. Kim, M. Kim, W. W. Bewley, *et al.*, "High-Power Single-Mode Distributed-Feedback Interband Cascade Lasers for the Midwave-Infrared," IEEE Photonics Technol. Lett. **19**(3), 158–160 (2007).
27. C. S. Kim, M. Kim, J. Abell, *et al.*, "Mid-infrared distributed-feedback interband cascade lasers with continuous-wave single-mode emission to 80 °C," Appl. Phys. Lett. **101**(6), 061104 (2012).
28. M. Carras, M. Garcia, X. Marcadet, *et al.*, "Top grating index-coupled distributed feedback quantum cascade lasers," Appl. Phys. Lett. **93**(1), 011109 (2008).
29. O. Cathabard, R. Teissier, J. Devenson, *et al.*, "InAs-based distributed feedback quantum cascade lasers," Electron. Lett. **45**(20), 1028–1030 (2009).
30. *COMSOL Multiphysics, version 6.2*, COMSOL AB, Stockholm, Sweden.
31. M. A. Ordal, R. J. Bell, R. W. Alexander, *et al.*, "Optical properties of Al, Fe, Ti, Ta, W, and Mo at submillimeter wavelengths," Appl. Opt. **27**(6), 1203 (1988).
32. M. A. Ordal, R. J. Bell, R. W. Alexander, *et al.*, "Optical properties of Au, Ni, and Pb at submillimeter wavelengths," Appl. Opt. **26**(4), 744 (1987).
33. H. Susanto Djie, C. Sookdhis, and P. Dowd, "Analysis and structure design of distributed-feedback laser (DFB) and distributed Bragg reflector (DBR) laser using regrowth-free surface grating technology," 250 (2001).
34. C. Ning, R.-X. Sun, S. Liu, *et al.*, "GaSb surface grating distributed feedback interband cascade laser emitting at 3.25 µm," Opt. Express **30**(16), 29007 (2022).
35. D. A. Díaz-Thomas, D. Ayache, M. Fagot, *et al.*, "Single mode, distributed feedback interband cascade lasers grown on Si for gas sensing," Appl. Phys. Lett. **126**(3), 031102 (2025).
36. K. Ikossi, M. Goldenberg, and J. Mittereder, "Metallization options and annealing temperatures for low contact resistance ohmic contacts to n-type GaSb," Solid-State Electron. **46**(10), 1627–1631 (2002).
37. A. Callegari, D. Lacey, and E. T.-S. Pan, "Electrical and thermal stability of AuGeNi ohmic contacts to GaAs fabricated with in situ RF sputter cleaning," Solid-State Electron. **29**(5), 523–527 (1986).